

Publisher: GSA  
Journal: GEOL: Geology  
Article ID: G35892

1 Global continental weathering trends across the Early  
2 Permian glacial to post-glacial transition: Correlating high  
3 and low paleo-latitude sedimentary records

4 **Jianghai Yang<sup>1\*</sup>, Peter A. Cawood<sup>2,3</sup>, Yuansheng Du<sup>1</sup>, Bin Feng<sup>4</sup>, and Jiaxin Yan<sup>1</sup>**

5 *<sup>1</sup>State Key Laboratory of Biogeology and Environmental Geology, China University of  
6 Geosciences, Wuhan, 430074, China*

7 *<sup>2</sup>Department of Earth Sciences, University of St. Andrews, North Street, St. Andrews KY16  
8 9AL, UK*

9 *<sup>3</sup>School of Earth and Environment, University of Western Australia, Crawley, WA 6009,  
10 Australia*

11 *<sup>4</sup>No.4 Institute of Geological & Mineral Resources Survey of Henan, Zhengzhou, 450016,  
12 China*

13 **ABSTRACT**

14 Time equivalent Early Permian sedimentary successions from high latitude  
15 Gondwana basins and from equatorial accumulations in North China, covering the glacial  
16 to post-glacial transition, display correlatable trends in continental weathering intensity  
17 based on chemical index of alteration (CIA) values. The successions display a pattern of  
18 CIA values that varies with latitude similar to modern estuarine suspended sediments.  
19 Based on the modern day CIA-temperature correlation, the syn-glacial early Permian low  
20 to high latitude land surface temperature gradient is estimated at ~20 °C, slightly higher  
21 than the calculated values for the contemporaneous sea surface temperature gradient.

22 **INTRODUCTION**

23           Chemical weathering displays a strong dependence on climate and is favored in hot  
24 and humid conditions, but depressed in cold and dry climates (Nesbitt and Young, 1982).  
25 It converts primary labile silicate minerals to secondary clay and oxide-hydroxide  
26 minerals, resulting in modified whole-rock elemental abundances (e.g., Nesbitt and  
27 Markovics, 1997). The chemical index of alteration (CIA, Nesbitt and Young, 1982) is the  
28 most widely accepted index and is based on the proportion of secondary aluminous  
29 minerals relative to primary mineral phases. CIA provides an effective measure of  
30 weathering conditions at the source.

31           In this paper we present mineralogical, geochemical and geochronological data  
32 from a Lower Permian sedimentary sequence in North China, documenting continental  
33 weathering trends in these low-latitude sedimentary rocks and correlate them with  
34 contemporaneous high-latitude Gondwana records. Furthermore, we show that modern  
35 day differences in chemical weathering intensities between the low- and high-latitude  
36 sediments can be applied to the earliest Permian successions, yielding realistic estimates of  
37 the land surface temperature gradient. The Early Permian marks the end of the major  
38 high-latitude Gondwana glaciation and the transition to a post-glaciation climate state  
39 (Fielding et al., 2008; Isbell et al., 2012). This transition coincides with changes in  
40 sedimentology, fossil assemblages and sediment composition (Dickins, 1996; Wopfner,  
41 1999), and with fluctuation in atmospheric CO<sub>2</sub> and O<sub>2</sub> contents (Glasspool and Scott,  
42 2010; Montañez et al., 2007).

#### 43 **GEOLOGICAL SETTING AND SAMPLING SEQUENCE**

44 The North China Craton occupied a near equatorial setting (~5–15 °) during the  
45 late Paleozoic (Fig. 1A; Huang et al., 2001). The craton formed through Paleoproterozoic  
46 suturing of Archean blocks and has constituted a stable platform since the  
47 Mesoproterozoic. Uplift in the early Paleozoic resulted in a major hiatus across the  
48 platform, and subsequent late Paleozoic transgression resulted in the deposition of  
49 widespread Late Carboniferous-Permian littoral, coal-bearing, clastic-dominated  
50 sequences (Wang, 1985). Drill core through the early Permian strata within the Yongcheng  
51 basin in southeastern North China yielded a continuous section that has escaped modern  
52 weathering. The sampled upper Shanxi Formation and conformably overlying Xiashihezi  
53 Formation consist of fine-grained sandstone, siltstone and black-pale gray mudstone with  
54 coal-seams up to several meters thick (Fig. 1b) that accumulated in a deltaic environment  
55 (Feng, 2012).

## 56 **Methods**

57 Whole-rock major and trace element concentrations were determined by XRF and  
58 ICP-MS, and mineralogical compositions were analyzed by XRD. Tuffaceous sandstone  
59 at the top Shanxi Formation was sampled for zircon LA-ICPMS dating. Analytical details  
60 and data are listed in the GSA Data Repository<sup>1</sup>.

## 61 **RESULTS**

62 Dated zircons are elongate and euhedral with well-developed oscillatory zoning  
63 (Fig. DR1A). Th/U ratios are 0.55–1.63, indicating a volcanic origin (Table DR1). The  
64 youngest 21 analyses with concordance of 95% or greater yielded an age of  $293.0 \pm 2.5$  Ma  
65 (MSWD = 0.57) (Fig. DR1B), and is interpreted as the crystallization age of the tuff. This

66 age constrains the Shanxi Formation to the **Asselian-Sakmarian** on the timescale of  
67 Gradstein et al. (2012).

68 Silt-mudstone samples are mainly composed of clay minerals and quartz, with little  
69 or no feldspar (0-6%) and calcite (0-2%) (Table DR2). High siderite contents occur in  
70 three samples. Identified clay minerals include kaolinite, chlorite and illite. Kaolinite  
71 displays a negative relation with both chlorite and illite, and increases significantly from  
72 50%–70% in the upper Shanxi Formation to 70%–80% in the lower Xiashihezi Formation  
73 (except for two samples with relatively high chlorite contents), and then decreases to  
74 40%–70% for most samples in the upper Xiashihezi Formation (Fig. DR2).

75 Calculated CIA values using the silica-bound calcium correction (Nesbitt and  
76 Young, 1982, Fedo et al., 1995; McLennan, 1993) for silt-mudstone samples show a sharp  
77 increase from 87.8 to 91.3 for the upper Shanxi Formation to 91.8–98.0 for the lower  
78 Xiashihezi Formation and then a gradual decrease to 81.7–92.0 for the upper Xiashihezi  
79 Formation. This variation is consistent with those of other weathering indices (e.g.,  
80 plagioclase index of alteration, Fedo et al., 1995) and kaolinite contents (Fig. DR2). Zr/Ti  
81 ratios, largely controlled by source rock composition (e.g., Scheffler et al., 2003), are  
82 relatively constant (Fig. DR2) and have no discernible co-variation with chemical  
83 weathering indices in the Lower Permian sequence. On the  $\text{Al}_2\text{O}_3\text{-CaO+Na}_2\text{O-K}_2\text{O}$   
84 (A-CN-K) plot (Nesbitt and Young, 1984; Fedo et al., 1995) (Fig. 1C), the samples with  
85 CIA values of < 86 trend approximately parallel to the A-CN boundary, mimicking the  
86 predicted weathering trend (Nesbitt and Young, 1984). Samples with higher CIA values  
87 (CIA > ~86) lie subparallel to the A-K boundary but gradually tend toward the A apex. On

88 the A-CN-K diagram the linear trend through the data points (sub)parallel to the A-CN  
89 boundary extends back to a point at which the proportion of plagioclase and K-feldspar are  
90 considered representative of the original parent rock composition (Fedo et al., 1995). This  
91 trend corresponds to the composition of the upper crust of southern North China (Gao et  
92 al., 1998) (Fig. 1C), the inferred source, and is consistent with facies reconstruction  
93 (Wang, 1985).

#### 94 **CORRELATIONS**

95 In the Early Permian, Gondwana occupied mid- to high southern hemisphere  
96 paleo-latitudes (Fig. 1, Torsvik and Cocks, 2004). Periodic glaciations are recorded in the  
97 sedimentary successions of the Karoo (Scheffler et al., 2006), Kalahari (Scheffler et al.,  
98 2006), Ruhuhu (Diekmann and Wopfner, 1996), Paraná (Goldberg and Humayun, 2010),  
99 Satpura (Roy and Roser, 2013), Khalaspir basins (Ghosh and Sarkar, 2010) and Spiti Basin  
100 (Ganai et al., 2014) (Fig. 1). End Carboniferous-Permian Gondwana successions in these  
101 basins all exhibit a significant CIA increase at the Early Permian glacial to post-glacial  
102 transition (Fig. 2), corresponding to the demise of the earliest Permian ice sheets (Isbell et  
103 al., 2012), and signify enhancement of continental weathering. This climatic event is  
104 constrained biostratigraphically to the **end Sakmarian-Artinskian** and by ion microprobe  
105 zircon dating in the Karoo Basin to around 290 Ma (Bangert et al., 1999). The elevated  
106 CIA values diminish by the **Kungurian**, around ~281 Ma on the basis of a zircon U-Pb age  
107 from the Paraná Basin (Mori et al., 2012).

108 Our new zircon age from the Yongcheng Basin indicates that the boundary  
109 between the Shanxi and Xiashihezi formations correlates, within error, with the glacial to

110 post-glacial transition in the Gondwana successions. This correlation indicates that the  
111 end-Sakmarian marks a significant rise in sediment CIA values in both low- and high-  
112 latitude locations and is a global signature (Fig. 2). The rise in CIA values also corresponds  
113 with an increase in atmospheric CO<sub>2</sub> content (Fig. 2; Montañez et al., 2007) and the global  
114 negative shift in seawater oxygen isotopes (Fig. 2; Korte et al., 2005; Korte et al., 2008). A  
115 subsequent decrease in CIA values is shown by both the North China and Gondwana  
116 sequences and has been related to intensifying aridity (Goldberg and Humayun, 2010)  
117 and/or a resumption of cold climate conditions (Fielding et al., 2008), and is accompanied  
118 by corresponding variation of atmospheric *p*CO<sub>2</sub> and seawater δ<sup>18</sup>O (Fig. 2).

## 119 **DISCUSSION**

120 Extrapolation of chemical proxy data to degree of weathering is influenced by  
121 sedimentary and tectonic processes (e.g., Rieu et al., 2007; Scheffler et al., 2003). The  
122 potential effect of such variables on weathering index of samples from the North China  
123 craton is minimized by the stable tectonic setting, the uniform source composition with  
124 derivation from within the craton, the absence of any evidence for significant potassium  
125 metasomatism (Fig. 1C), and analyses limited to lutite samples from fresh core. Therefore,  
126 chemical weathering index signatures and linked clay mineral assemblage variation  
127 provide a valid record of changes in chemical weathering conditions of the source related  
128 to climate variation. Greatly enhanced continental weathering during the deposition of the  
129 basal Xiashihezi Formation corresponds with basin deepening and a major marine  
130 transgression (Feng, 2012), consistent with the intensification of weathering and a  
131 post-glacial climate. Temporal correlation of the continental weathering trends in North

132 China with similar trends in Gondwana indicates a global phenomenon recording the  
133 glacial to post-glacial transition (Fig. 2), despite possible local tectonic influences on  
134 sediments, which might be averaged out by large catchment areas for the sampled basins.  
135 This event corresponds to a warming interval associated with high atmospheric CO<sub>2</sub>  
136 concentrations (up to 2500 ppmv), which are distinctly higher than the earliest Permian  
137 values (~300 ppmv) of averaged present atmospheric CO<sub>2</sub> levels and followed by a  
138 short-lived drop in the Artinskian (Montañez et al., 2007). **Increasing temperature is**  
139 **characteristic of a glacial to post-glacial transition (Korte et al., 2008; Rieu et al., 2007).**  
140 **Such a CO<sub>2</sub>-forcing climate change could be responsible for the continental weathering**  
141 **enhancement as manifested by the compiled sediment geochemical data (Fig. 2).**

142 Modern large river estuary suspended sediment analyses show CIA values  
143 changing with latitude and land surface temperature (Li and Yang, 2010). We hypothesize  
144 a similar latitude-associated silicate weathering distribution in the earliest Permian  
145 glaciation, which is an interval with atmospheric CO<sub>2</sub> levels broadly similar to the present  
146 day average (Montañez et al., 2007). CIA-latitude and CIA-temperature correlations for  
147 modern estuary systems are depicted in figure 3, and North China and Gondwana basin  
148 data are also plotted on this diagram based on their CIA values. The obtained latitude  
149 ranges overlap with those determined from Early Permian paleogeographic constraints  
150 (Fig. 1, Torsvik and Cocks, 2004). Given this relationship, we estimate a low- to  
151 high-latitude land surface temperature (LST) gradient of ~20 °C and mid- to high-latitude  
152 LST gradient of ~10 °C for the earliest Permian glacial stage. The low- to high-latitude  
153 LST gradient is largely comparable with the result based on present day CO<sub>2</sub> concentration

154 modeled by Gibbs et al. (2002) for the Sakmarian, but higher than the contemporaneous  
155 low- to high-latitude sea surface temperature gradient of ~9–12 °C given by Korte et al.  
156 (2008), likely reflecting differences in the heat transport efficiency between the oceans and  
157 the atmosphere. The smaller difference in CIA values between the post-glacial low- and  
158 high-latitude basins (Fig. 2) likely denotes a subdued temperature gradient during that  
159 period.

## 160 **CONCLUSIONS**

161 A tuff zircon age and variations in CIA values from the Lower Permian sequence in  
162 North China enable correlation of this low-latitude sedimentary record with those in  
163 high-latitude Gondwana regions. Concomitant offset toward high CIA values in both high  
164 and low latitudinal successions reflects global climate change from a glacial to post-glacial  
165 state. Correlations of continental weathering with latitude and with temperature based on  
166 models from present day settings demonstrate a low- to high-latitude LST gradient of ~20  
167 °C for the earliest Permian syn-glacial period.

## 168 **ACKNOWLEDGMENTS**

169 Editor Ellen Thomas and reviewers Grant M. Young, Karin Goldberg, Lorenz  
170 Schwark and Isabel P. Montañez are gratefully acknowledged for their constructive  
171 comments. We thank Zhaochu Hu for help with zircon LA-ICPMS dating and staff at  
172 the Yongcheng County core storage facility for help with sampling. This study was  
173 financially supported by National Science Foundation of China (Nos. 40921062 and  
174 41302083), the ‘111project’ (No. B08030) and the Fundamental Research Funds for  
175 the Central Universities (CUGL140402).



176 **REFERENCES CITED**

- 177 Bangert, B., Stollhofen, H., Lorenz, V., and Armstrong, R., 1999, The geochronology and  
178 significance of ash-fall tuffs in the glaciogenic Carboniferous-Permian Dwyka Group  
179 of Namibia and South Africa: *Journal of African Earth Sciences*, v. 29, p. 33–49,  
180 doi:10.1016/S0899-5362(99)00078-0.
- 181 Dickins, J.M., 1996, Problems of a Late Paleozoic glaciation in Australia and subsequent  
182 climate in the Permian: *Palaeogeography, Palaeoclimatology, Palaeoecology*, v. 125,  
183 p. 185–197, doi:10.1016/S0031-0182(96)00030-2.
- 184 Diekmann, B., and Wopfner, H., 1996, Petrographic and diagenetic signatures of climatic  
185 change in peri- and postglacial Karoo Sediments of SW Tanzania: *Palaeogeography,*  
186 *Palaeoclimatology, Palaeoecology*, v. 125, p. 5–25,  
187 doi:10.1016/0031-0182(95)00084-4.
- 188 Fedo, C.M., Nesbitt, H.W., and Young, G.M., 1995, Unraveling the effects of potassium  
189 metasomatism in sedimentary rocks and paleosols, with implications for  
190 paleoweathering conditions and provenance: *Geology*, v. 23, p. 921–924,  
191 doi:10.1130/0091-7613(1995)023<0921:UTEOPM>2.3.CO;2.
- 192 Feng, B., 2012, Study on coal-accumulating characteristic of Shanxi Formation and low  
193 Shihezi Formation in Yongcheng Coalfield: Henna Province: *Journal of Henan*  
194 *Polytechnic University*, v. 31, p. 177–181.
- 195 Fielding, C.R., Frank, T.D., Birgenheiner, L.P., Rygel, M.C., Jones, A.J., and Roberts, J.,  
196 2008, Stratigraphic imprint of the Late Paleozoic Ice Age in eastern Australia: A

- 197 record of alternating glacial and nonglacial climate regime: *Journal of the Geological*  
198 *Society*, v. 165, p. 129–140, doi:10.1144/0016-76492007-036.
- 199 Ganai, J.A., Rashid, S.A., Alam, M.M., Balaram, V., and Sathyanarayanan, M., 2014, The  
200 geochemistry of Permo-Carboniferous black shales from Spiti region, Himachal  
201 Pradesh, Tethys Himalaya: A record of provenance and change in climate: *Himalayan*  
202 *Geology*, v. 35, no. 1, p. 31–39.
- 203 Gao, S., Luo, T., Zhang, B., Zhang, H., Han, Y., Zhao, Z., and Hu, Y., 1998, Chemical  
204 composition of the continental crust as revealed by studies in East China: *Geochimica*  
205 *et Cosmochimica Acta*, v. 62, p. 1959–1975, doi:10.1016/S0016-7037(98)00121-5.
- 206 Ghosh, S., and Sarkar, S., 2010, Geochemistry of Permo-Triassic mudstone of the Satpura  
207 Gondwana basin, central India: Clues for provenance: *Chemical Geology*, v. 277,  
208 p. 78–100, doi:10.1016/j.chemgeo.2010.07.012.
- 209 Gibbs, M.T., Rees, P.M., Kutzbach, J.E., Ziegler, A.M., Behling, P.J., and Rowley, D.B.,  
210 2002, Simulations of Permian climate and comparisons with climate-sensitive  
211 sediments: *The Journal of Geology*, v. 110, p. 33–55, doi:10.1086/324204.
- 212 Goldberg, K., and Humayun, M., 2010, The applicability the Chemical Index of Alteration  
213 as a paleoclimatic indicator: An example from the Permian of the Paraná Basin,  
214 Brazil: *Palaeogeography, Palaeoclimatology, Palaeoecology*, v. 293, p. 175–183,  
215 doi:10.1016/j.palaeo.2010.05.015.
- 216 Glasspool, I.J., and Scott, A.C., 2010, Phanerozoic concentrations of atmospheric oxygen  
217 reconstructed from sedimentary charcoal: *Nature Geoscience*, v. 3, p. 627–630,  
218 doi:10.1038/ngeo923.

- 219 Gradstein, F.M., Ogg, J.G., Schmitz, M.D., and Ogg, G.M., 2012, The geological time  
220 scale 2012: Oxford, UK, Elsevier, p. 1144.
- 221 Huang, B., Otofujii, Y.I., Zhu, R., Shi, R., and Wang, Y., 2001, Paleomagnetism of  
222 Carboniferous sediments in the Hexi corridor: Its origin and tectonic implications:  
223 Earth and Planetary Science Letters, v. 194, p. 135–149,  
224 doi:10.1016/S0012-821X(01)00557-X.
- 225 Isbell, J.L., Henry, L.C., Gulbranson, E.L., Limarino, C.O., Fraiser, M.L., Koch, Z.J.,  
226 Ciccioli, P.L., and Dineen, A.A., 2012, Glacial paradoxes during the late Paleozoic ice  
227 age: evaluating the equilibrium line altitude as a control on glaciation: Gondwana  
228 Research, v. 22, p. 1–19, doi:10.1016/j.gr.2011.11.005.
- 229 Korte, C., Jasper, T., Kozur, H.W., and Veizer, J., 2005,  $\delta^{18}\text{O}$  and  $\delta^{13}\text{C}$  of Permian  
230 branchiopods: A record of seawater evolution and continental glaciation:  
231 Palaeogeography, Palaeoclimatology, Palaeoecology, v. 224, p. 333–351,  
232 doi:10.1016/j.palaeo.2005.03.015.
- 233 Korte, C., Jones, P.J., Brand, U., Mertmann, D., and Veizer, J., 2008, Oxygen isotope  
234 values from high-latitudes: Clues for Permian sea-surface temperature gradients and  
235 late Paleozoic deglaciation: Palaeogeography, Palaeoclimatology, Palaeoecology,  
236 v. 269, p. 1–16, doi:10.1016/j.palaeo.2008.06.012.
- 237 Li, C., and Yang, S., 2010, Is chemical index of alteration (CIA) a reliable proxy for  
238 chemical weathering in global drainage basins?: American Journal of Science, v. 310,  
239 p. 111–127, doi:10.2475/02.2010.03.
- 240 Mahjoor, A.S., Karimi, M., and Rastegarlar, A., 2009, Mineralogical and geochemical

- 241 characteristics of clay deposits from South Abarkouh district of clay deposit (Central  
242 Iran) and their applications: *Journal of Applied Science*, v. 9, no. 4, p. 601–614,  
243 doi:10.3923/jas.2009.601.614.
- 244 McLennan, S.M., 1993, Weathering and global denudation: *The Journal of Geology*,  
245 v. 101, p. 295–303, doi:10.1086/648222.
- 246 Montañez, I.P., Tabor, N.J., Niemeier, D., DiMichele, W.A., Frank, T.D., Fielding, C.R.,  
247 Isbell, J.L., Birgenheier, L.P., and Rygel, M.C., 2007, CO<sub>2</sub>-forced climate and  
248 vegetation instability during Late Paleozoic deglaciation: *Science*, v. 315, p. 87–91,  
249 doi:10.1126/science.1134207.
- 250 Mori, A.L.O., de-Souza, P.A., Marques, J.C., and Lopes, R.C., 2012, A new U-Pb zircon  
251 age dating and palynological data from a Lower Permian section of the southernmost  
252 Paraná Basin, Brazil: biochronostratigraphical and geochronological implications for  
253 Gondwanan correlations: *Gondwana Research*, v. 21, p. 654–669,  
254 doi:10.1016/j.gr.2011.05.019.
- 255 Nesbitt, H.W., and Markovics, G., 1997, Weathering of granodioritic crust, long-term  
256 storage of elements in weathering profiles, and petrogenesis of siliciclastic sediments:  
257 *Geochimica et Cosmochimica Acta*, v. 61, p. 1653–1670,  
258 doi:10.1016/S0016-7037(97)00031-8.
- 259 Nesbitt, H.W., and Young, G.M., 1982, Early Proterozoic climates and plate motions  
260 inferred from major element chemistry of lutites: *Nature*, v. 299, p. 715–717,  
261 doi:10.1038/299715a0.

- 262 Nesbitt, H.W., and Young, G.M., 1984, Prediction of some weathering trends of plutonic  
263 and volcanic rocks based on thermodynamic and kinetic considerations: *Geochimica*  
264 *et Cosmochimica Acta*, v. 48, p. 1523–1534, doi:10.1016/0016-7037(84)90408-3.
- 265 Rieu, R., Allen, P.A., Plötze, M., and Pettke, T., 2007, Climatic cycles during a  
266 Neoproterozoic “snowball” glacial epoch: *Geology*, v. 35, p. 299–302,  
267 doi:10.1130/G23400A.1.
- 268 Roy, D.K., and Roser, B.P., 2013, Climatic control on the composition of  
269 Carboniferous-Permian Gondwana sediments, Khalaspir basin, Bangladesh:  
270 *Gondwana Research*, v. 23, p. 1163–1171, doi:10.1016/j.gr.2012.07.006.
- 271 Scheffler, K., Hoernes, S., and Schwark, L., 2003, Global changes during  
272 Carboniferous-Permian glaciation of Gondwana: linking polar and equatorial climate  
273 evolution by geochemical proxies: *Geology*, v. 31, p. 605–608,  
274 doi:10.1130/0091-7613(2003)031<0605:GCDCGO>2.0.CO;2.
- 275 Scheffler, K., Buehmann, D., and Schwark, L., 2006, Analysis of late Paleozoic glacial to  
276 postglacial sedimentary successions in South Africa by geochemical  
277 proxies—response to climate evolution and sedimentary environment:  
278 *Palaeogeography, Palaeoclimatology, Palaeoecology*, v. 240, p. 184–203,  
279 doi:10.1016/j.palaeo.2006.03.059.
- 280 Taylor, S.R., and McLennan, S.M., 1985, *The continental crust: Its composition and*  
281 *evolution*: Oxford, United Kingdom, Blackwell, 1–312 p.

- 282 Torsvik, T.H., and Cocks, L.R.M., 2004, Earth geography from 400 to 250 Ma: a  
283 paleomagnetic, faunal and facies review: *Journal of the Geological Society*, v. 161,  
284 p. 555–572, doi:10.1144/0016-764903-098.
- 285 Wang, H., 1985, *Atlas of the palaeogeography of China*: Beijing, Cartographic Publishing  
286 House, 74–80 p.
- 287 Wopfner, H., 1999, The Early Permian deglaciation event between East Africa and  
288 northwestern Australia: *Journal of African Earth Sciences*, v. 29, p. 77–90,  
289 doi:10.1016/S0899-5362(99)00081-0.

## 290 **FIGURE CAPTIONS**

291 Figure 1. (A) Magneto- and fauna-based Early Permian paleogeographic map (Huang et  
292 al., 2001; Torsvik and Cocks, 2004) showing the approximate positions of the Yongcheng  
293 (black square) and the Gondwana basins (black stars: 1-Satpura Basin, 2-Khalaspir Basin,  
294 3-Kalahari Basin, 4-Ruhuhu Basin, 5-Paraná Basin, 6-Karoo Basin, 7-Spiti Basin and  
295 8-Central Iran Basin); (B) stratigraphic column of Core Zk1401 with analyzed samples,  
296 where filled circles, blank circles and filled star represent silt-mudstone, fine-grained  
297 sandstone and zircon dating sample sites, respectively; and (C) A-CN-K  
298 ( $\text{Al}_2\text{O}_3\text{-CaO}^*\text{+Na}_2\text{O-K}_2\text{O}$ ) diagram for the Lower Permian silt-mudstone (open circles)  
299 and fine-grained sandstone (open diamonds) samples, with CIA scale on the left side. Also  
300 plotted are the molar proportions of southern North China upper crust (SCN, Gao et al.,  
301 1998), interior North China upper crust (INC, Gao et al., 1998) and average upper  
302 continental crust (UCC, Taylor and McLennan, 1985).

303 Figure 2. Correlating CIA variation of the equatorial Early Permian pelitic sedimentary  
304 rocks from the Yongcheng Basin in North China with those from the mid-high latitude  
305 Khalaspir Basin (Roy and Roser, 2013), Satpura Basin (Ghosh and Sarkar, 2010), Karoo  
306 Basin (Scheffler et al., 2006), Kalahari Basin (Scheffler et al., 2006), Ruhuhu Basin  
307 (Diekmann and Wopfner, 1996), Paraná Basin (Goldberg and Humayun, 2010), Spiti  
308 Basin (Ganai et al., 2014) and Central Iran Basin (Mahjoor et al., 2009) in Gondwana. The  
309 zircon age data obtained by this study for the Yongcheng sequence, by Bangert et al.  
310 (1999) for the Karoo sequence, and by Mori et al. (2012) for the Paraná sequence, are  
311 marked according to their respective stratigraphic positions. Also shown are the temporal  
312 variations in inferred atmospheric CO<sub>2</sub> content (Montañez et al., 2007) and low- and high-  
313 latitudinal low-Mg calcite oxygen isotopic signature from fossil shells for comparison  
314 (Korte et al., 2005; Korte et al., 2008).

315 Figure 3. Plot of mean CIA values (green line) and deviations (gray box) for each of the  
316 studied and compiled earliest Permian sedimentary rocks with those from modern estuary  
317 suspended sediment CIA-latitude (A) and CIA-temperature (B) correlation models based  
318 on the compilation (black squares) of Li and Yang (2010). Abbreviations: YB-Yongcheng  
319 Basin, SB-Satpura Basin, SIB-Spiti Basin, PB-Paraná Basin, KB-Karoo Basin,  
320 KLB-Khalaspir Basin, and RB-Ruhuhu Basin.

321 <sup>1</sup>GSA Data Repository item 2014xxx, xxxxxxxx, is available online at  
322 [www.geosociety.org/pubs/ft2014.htm](http://www.geosociety.org/pubs/ft2014.htm), or on request from [editing@geosociety.org](mailto:editing@geosociety.org) or  
323 Documents Secretary, GSA, P.O. Box 9140, Boulder, CO 80301, USA.

Figure 1  
[Click here to download high resolution image](#)

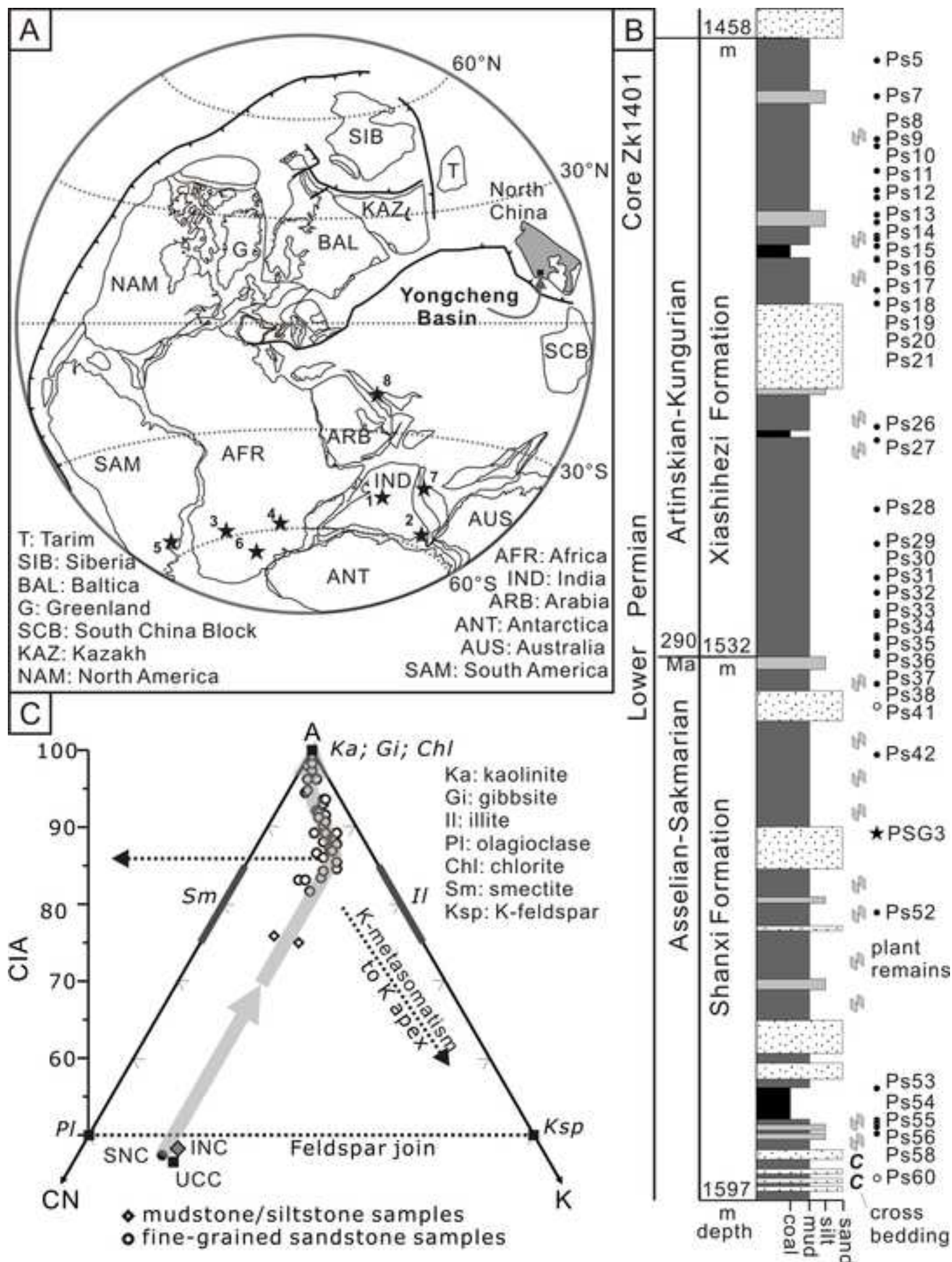




Figure 2  
[Click here to download high resolution image](#)

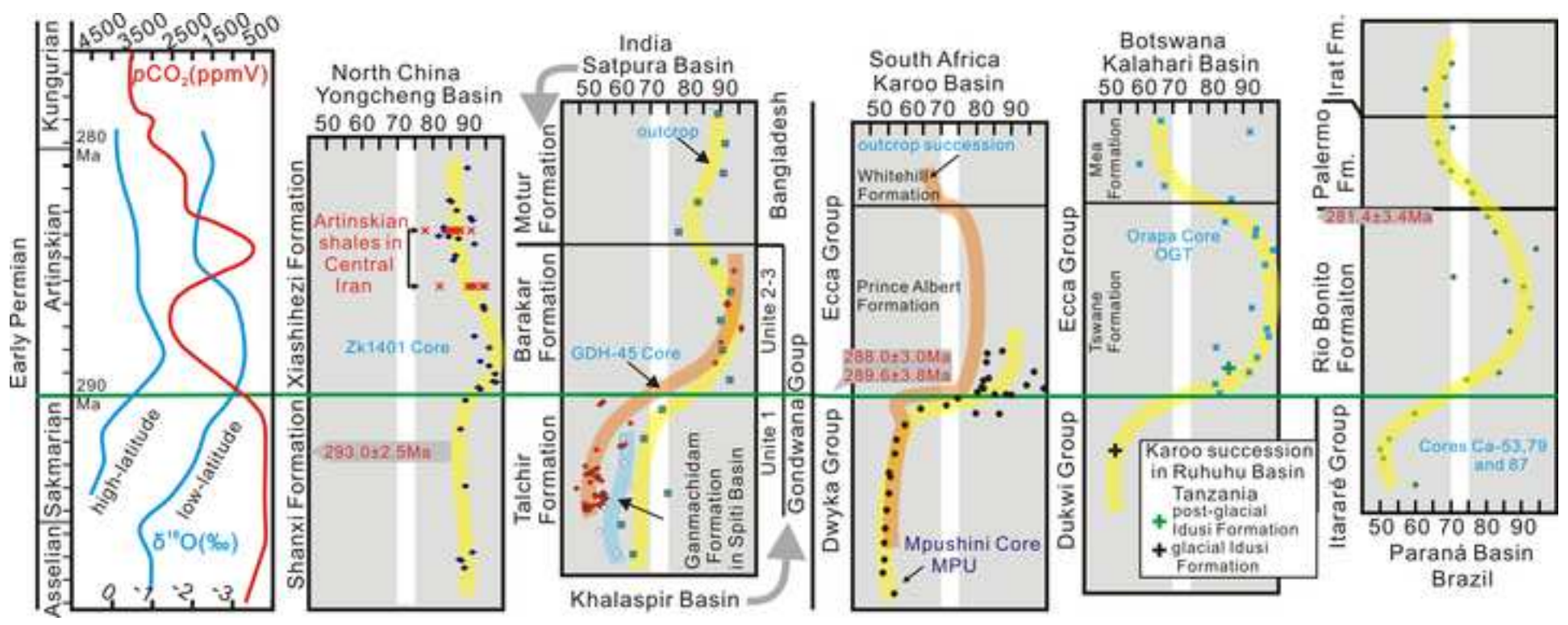
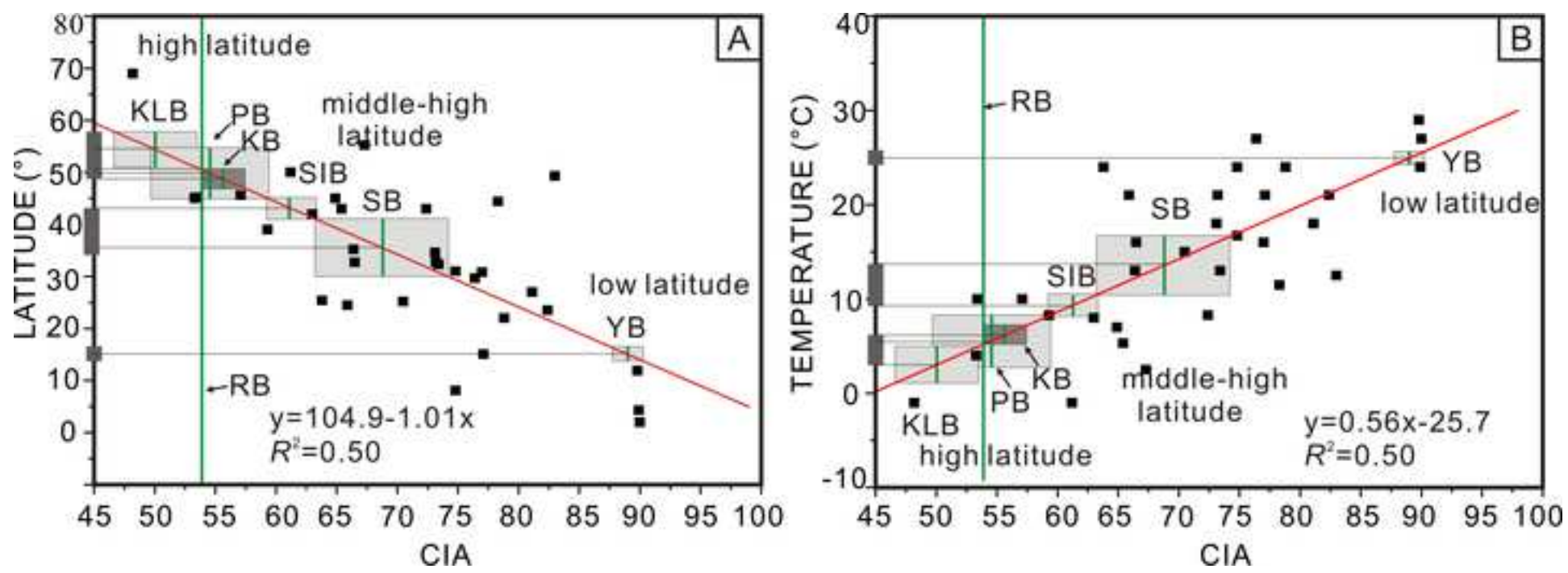


Figure 3  
[Click here to download high resolution image](#)



## GSA Data repository Item

Supplementary materials for:

### **Global continental weathering trends across the Early Permian glacial to postglacial transition: Correlating high and low paleo-latitude sedimentary records**

Jianghai Yang<sup>1\*</sup>, Peter A. Cawood<sup>2,3</sup>, Yuansheng Du<sup>1</sup>, Bin Feng<sup>4</sup>, Jiaxin Yan<sup>1</sup>,

<sup>1</sup> State Key Laboratory of Biogeology and Environmental Geology, China University of Geosciences, Wuhan, 430074, China

<sup>2</sup> Department of Earth Sciences, University of St. Andrews, North Street, St. Andrews KY16 9AL, UK

<sup>3</sup> School of Earth and Environment, University of Western Australia, Crawley, WA 6009, Australia

<sup>4</sup> No.4 Institute of Geological & Mineral Resources Survey of Henan, Zhengzhou, 450016, China

#### **ANALYTICAL PROCEDURES**

Whole-rock major and trace element concentrations were determined with X-ray fluorescence and ICP-MS by ALS Chemex, and mineralogical X-Ray Diffraction analysis and zircon LA-ICPMS dating were conducted in the State Key Laboratory of Geological Process and Mineral Resources, China University of Geosciences (Wuhan).

##### **1. U-Pb isotope LA-ICPMS analysis of zircons**

Zircons were separated from sample PSG3 by conventional procedures before hand-picking under a binocular microscope, mounting in epoxy and polished. Back scatter electron (BSE) and cathodoluminescence (CL) images were conducted on a JEOL JXA-8100 electron microprobe. Representative CL images for the analyzed zircons are shown in Figure DR1. Prior to LA-ICPMS analysis, zircons were subject to washing with dilute HNO<sub>3</sub> in an ultrasonic bath to eliminate surface contamination. For the LA-ICPMS analyses, laser sampling was performed using a Geolas 2005, and ion-signal intensities were acquired by an Agilent 7500a ICP-MS instrument. The diameter of the laser spot was 32 μm. Each analysis incorporated a background acquisition of approximately 20-30 s (gas blank) followed by 50 s data acquisition from the sample. The Agilent Chemstation was utilized for the acquisition of each individual analysis. Detailed operating conditions for the laser ablation system and the ICP-MS instrument and data reduction are described by Liu et al. (2010). Zircon 91500 (<sup>206</sup>Pb/<sup>238</sup>U age = 1062.4 ± 0.4 Ma, Wiedenbeck et al., 1995) was used as external standard for U-Pb dating, and was analyzed twice every 6 analyses. Off-line selection and integration of background and signals, and time-drift correction and quantitative calibration for trace element analyses and U-Pb dating were performed by ICPMSDataCal (Liu et al., 2010; Liu et al., 2008). Concordia diagrams and weighted mean calculations were made using Isoplt/Ex\_ver3 (Ludwig, 2003). Zircon standards GJ-1 was analyzed as unknown and the obtained mean <sup>206</sup>Pb/<sup>238</sup>U age is 599.1 ± 8.4 Ma (2σ) in line with the recommended age of 599.8 ± 1.7 Ma (2σ, Jackson et al., 2004).

## **2. Mineralogical X-Ray Diffraction analysis**

X-ray diffraction (XRD) studies of samples were performed with a PANalytical X'Pert Pro using a Cu-Ni tube at 40 kV and 40 mA, under continuous scanning with a speed of 8°/min. The mass percentage (mass %) of the main mineral phases identified were semi-quantified with an analytical error of  $\pm 10\%$ .

## **3. Whole-rock geochemical analysis**

After removing surface layer, solid samples were grounded to less than 200 mesh. For elemental oxide concentration analysis, sample powders were mixed with dry lithium tetraborate and borate and fused to glass beads, and analytical performance was conducted on a PANalytical Axios X-ray fluorescence spectrometer with accuracy better than 5% and uncertainty less than 5%. Trace element (Rb, Sr, Ba, and Zr) contents were obtained on Perkin Elmer Elan 9000 ICP-MS with accuracy better than 10% and uncertainty less than 10% for the analyzed elements after complete fusion of samples with lithium borate and dissolution in ultrapure HNO<sub>3</sub>.

## DATA REPOSITORTY FIGURE CAPTIONS

**Figure DR1.** A: Representative CL images for dated zircons; B: Tera-Wasserburg plot of zircon analyses from Sample PGS3, where the gray symbols mark the integrated analyses for calculating weighted average age [inset,  $293.0 \pm 2.5$  Ma ( $n = 21$ ,  $MSWD = 0.57$ )]. This average age is equal to the lower intercept age within error ( $290.0 \pm 3.0$  Ma) and interpreted as the depositional age of this tuffaceous bed. Another three concordant analyses gave Paleoproterozoic  $^{207}\text{Pb}/^{206}\text{Pb}$  ages (1832-1721 Ma, Table DR1), and are considered xenocrystic in origin.

**Figure DR2.** Stratigraphic variations of CIA value (chemical index of alteration, Nesbitt and Young, 1982), clay mineral assemblage, and provenance chemical indicator Zr/Ti ratio for silt-mudstone samples. Other chemical weathering indices including weathering index of Parker (WIP, Parker, 1970), chemical index of weathering (CIW, Harnois, 1988), plagioclase index of alteration (PIA, Fedo et al., 1995) and  $\text{CIA}_{\text{molar}}$  (expressed as  $\text{Al}_2\text{O}_3/(\text{CaO}^* + \text{Na}_2\text{O} + \text{K}_2\text{O})$  mole ratio, Goldberg and Humayun, 2010) were also plotted for comparison.  $\text{CaO}^*$  involved in index calculations represent only the Ca in silicate fractions.

## REFERENCES CITED

- Goldberg, K., and Humayun, M., 2010, The applicability the Chemical Index of Alteration as a paleoclimatic indicator: an example from the Permian of the Paraná Basin, Brazil: *Palaeogeography, Palaeoclimatology, Palaeoecology*, v. 293, p. 175-183.
- Harnois, L., 1988, The CIW index: a new chemical index of weathering: *Sedimentary Geology*, v. 55, p. 319-322.
- Jackson SE, Pearson NJ, Griffin WL, Belousova EA. 2004. The application of laser ablation-inductively coupled plasma-mass spectrometry to in situ U-Pb zircon geochronology. *Chemical Geology*, v. 211, p. 47-69.
- Liu, Y., Gao, S., Hu, Z., Gao, C., and Zong, K., 2010, Continental and oceanic crust recycling-induced melt-peridotite interactions in the Trans-North China Orogen: U-Pb dating, Hf isotopes and trace elements in zircons of mantle xenoliths: *Journal of Petrology*, v. 51, p. 537-571.
- Liu, Y., Zong, K., Kelemen, P.B., and Gao, S., 2008, Geochemistry and magmatic history of eclogites and ultramafic rocks from the Chinese continental scientific drill hole: subduction and ultrahigh-pressure metamorphism of lower crustal cumulates: *Chemical Geology*, v. 247, p. 133-153.
- Nesbitt, H.W., and Young, G.M., 1982, Early Proterozoic climates and plate motions inferred from major element chemistry of lutites: *Nature*, v. 299, p. 715-717.
- , 1984, Prediction of some weathering trends of plutonic and volcanic rocks based on thermodynamic and kinetic considerations: *Geochimica et Cosmochimica Acta*, v. 48, p. 1523-1534.
- Ludwig K.R. 2003. User`s manual for Isoplot 3.00: a geochronological toolkit for microsoft Excel: Berkeley
- Parker, A., 1970, An index of weathering for silicate rocks: *Geological Magazine*, v. 107, p. 501-504.
- Wiedenbeck, M., Allé, P., Corfu, F., Griffin, W.L., Meier, M., Oberli, F., von Quadt, A., Roddick, J.C, Spiegel, W., 1995. Three natural zircon standards for U-Th-Pb, Lu-Hf, trace element and REE analyses. *Geostand. Newsl.*, v. 19, p.1-23.

**Table DR1.** Zircon U-Pb isotope data for tuffaceous sandstone Sample PSG3

Spot	Pb	Th	U	Th/U	207Pb/206Pb		207Pb/235U		206Pb/238U		rho	207Pb/206Pb		207Pb/235U		206Pb/238U		Concordance
	ppm	ppm	ppm		Ratio	±1σ	Ratio	±1σ	Ratio	±1σ		Age (Ma)	±1σ	Age (Ma)	±1σ	Age (Ma)	±1σ	
PSG3-1	45.0	119	132	0.90	0.0550	0.0045	0.3649	0.0262	0.0499	0.0010	0.2875	409	183	316	20	314	6	99%
PSG3-2	18.0	84.0	118	0.71	0.0572	0.0041	0.3602	0.0254	0.0459	0.0008	0.2529	498	159	312	19	289	5	92%
PSG3-3	27.9	134	152	0.88	0.0542	0.0047	0.3377	0.0283	0.0458	0.0010	0.2565	389	196	295	21	289	6	97%
PSG3-4	18.6	91.8	108	0.85	0.0540	0.0050	0.3337	0.0299	0.0459	0.0010	0.2347	372	209	292	23	289	6	98%
PSG3-5	21.1	108	118	0.92	0.0554	0.0037	0.3524	0.0242	0.0465	0.0011	0.3460	428	150	307	18	293	7	95%
PSG3-6	31.8	149	183	0.81	0.0476	0.0031	0.3177	0.0207	0.0487	0.0010	0.3071	80	148	280	16	306	6	91%
PSG3-7	23.4	107	132	0.81	0.0526	0.0040	0.3240	0.0239	0.0460	0.0010	0.3002	322	174	285	18	290	6	98%
PSG3-8	22.6	102	126	0.82	0.0520	0.0033	0.3276	0.0208	0.0465	0.0010	0.3440	283	153	288	16	293	6	98%
PSG3-9	18.7	77.3	121	0.64	0.0663	0.0051	0.4525	0.0374	0.0504	0.0015	0.3526	817	156	379	26	317	9	82%
PSG3-10	112	74.2	97.8	0.76	0.1122	0.0036	5.3605	0.1810	0.3461	0.0048	0.4117	1836	59	1879	29	1916	23	98%
PSG3-11	31.4	150	208	0.72	0.0535	0.0038	0.3402	0.0223	0.0476	0.0010	0.3246	346	163	297	17	300	6	99%
PSG3-12	15.6	69.9	111	0.63	0.0558	0.0044	0.3649	0.0277	0.0479	0.0011	0.3110	443	174	316	21	302	7	95%
PSG3-13	19.9	95.6	127	0.75	0.0539	0.0049	0.3422	0.0298	0.0475	0.0012	0.2870	369	206	299	23	299	7	99%
PSG3-14	19.4	80.0	134	0.60	0.0623	0.0046	0.3941	0.0284	0.0465	0.0010	0.2967	687	158	337	21	293	6	85%
PSG3-15	12.8	60.0	84.9	0.71	0.0637	0.0059	0.4135	0.0366	0.0475	0.0012	0.2839	731	196	351	26	299	7	83%
PSG3-16	18.4	83.4	90.6	0.92	0.0815	0.0068	0.5083	0.0423	0.0455	0.0012	0.3134	1235	165	417	28	287	7	63%
PSG3-17	20.1	85.1	154	0.55	0.0568	0.0044	0.3708	0.0269	0.0482	0.0010	0.3007	483	175	320	20	304	6	94%
PSG3-18	12.9	58.3	87.8	0.66	0.0522	0.0049	0.3385	0.0312	0.0482	0.0012	0.2647	300	217	296	24	303	7	97%
PSG3-19	12.8	51.8	80.6	0.64	0.0629	0.0053	0.4089	0.0344	0.0473	0.0011	0.2792	706	175	348	25	298	7	84%
PSG3-20	16.3	80.5	108	0.74	0.0563	0.0046	0.3724	0.0330	0.0478	0.0011	0.2689	465	183	321	24	301	7	93%
PSG3-21	18.6	88.0	125	0.71	0.0541	0.0042	0.3450	0.0263	0.0465	0.0011	0.3014	376	174	301	20	293	7	97%
PSG3-22	17.7	83.8	93.7	0.89	0.0704	0.0060	0.4387	0.0346	0.0478	0.0012	0.3220	939	176	369	24	301	7	79%
PSG3-23	21.6	92.4	143	0.65	0.0578	0.0048	0.3761	0.0306	0.0470	0.0009	0.2271	524	183	324	23	296	5	90%
PSG3-24	142	717	571	1.26	0.0568	0.0025	0.3671	0.0169	0.0463	0.0007	0.3408	483	103	318	13	292	4	91%
PSG3-25	15.0	66.0	90.8	0.73	0.0569	0.0055	0.3545	0.0305	0.0474	0.0012	0.2930	487	215	308	23	298	7	96%
PSG3-26	11.3	54.0	91.8	0.59	0.0679	0.0063	0.4446	0.0374	0.0486	0.0012	0.2985	878	194	373	26	306	8	80%
PSG3-27	15.2	75.6	110	0.69	0.0636	0.0053	0.3785	0.0288	0.0445	0.0010	0.2839	728	177	326	21	281	6	85%
PSG3-28	29.6	143	203	0.71	0.0543	0.0037	0.3351	0.0213	0.0456	0.0009	0.3201	383	149	293	16	288	6	98%
PSG3-29	16.6	77.4	114	0.68	0.0570	0.0050	0.3636	0.0295	0.0481	0.0011	0.2785	500	193	315	22	303	7	96%
PSG3-30	13.5	53.9	74.5	0.72	0.0638	0.0056	0.3996	0.0344	0.0464	0.0012	0.3001	744	185	341	25	293	7	84%
PSG3-31	15.3	75.2	117	0.64	0.0531	0.0036	0.3286	0.0213	0.0456	0.0010	0.3375	345	154	288	16	288	6	99%
PSG3-32	37.7	167	228	0.73	0.0557	0.0033	0.3577	0.0212	0.0471	0.0008	0.2980	439	135	310	16	296	5	95%
PSG3-33	12.5	52.9	75.6	0.70	0.0693	0.0058	0.4443	0.0378	0.0469	0.0014	0.3402	906	173	373	27	295	8	76%
PSG3-34	20.2	88.0	124	0.71	0.0593	0.0046	0.3635	0.0251	0.0462	0.0010	0.3091	589	136	315	19	291	6	92%

PSG3-35	11.5	54.7	74.3	0.74	0.0663	0.0068	0.3956	0.0388	0.0446	0.0011	0.2584	817	214	338	28	281	7	81%
PSG3-36	58.1	34.8	77.9	0.45	0.1063	0.0043	4.7052	0.1983	0.3210	0.0054	0.4027	1737	74	1768	35	1794	27	98%
PSG3-37	28.9	136	136	1.00	0.0553	0.0044	0.3620	0.0273	0.0484	0.0011	0.3142	433	181	314	20	305	7	97%
PSG3-38	19.6	31.5	43.0	0.73	0.2131	0.0192	1.6076	0.1256	0.0582	0.0022	0.4861	2929	146	973	49	365	13	9%
PSG3-39	33.9	161	165	0.97	0.0600	0.0042	0.3724	0.0255	0.0458	0.0010	0.3051	611	154	321	19	288	6	89%
PSG3-40	18.6	88.8	115	0.78	0.0537	0.0045	0.3446	0.0268	0.0469	0.0008	0.2294	361	189	301	20	295	5	98%
PSG3-41	41.7	205	223	0.92	0.0579	0.0034	0.3616	0.0206	0.0453	0.0008	0.3154	528	130	313	15	286	5	90%
PSG3-42	14.7	72.1	96.8	0.74	0.0592	0.0053	0.3676	0.0324	0.0460	0.0012	0.2842	576	199	318	24	290	7	90%
PSG3-43	25.3	130	107	1.21	0.0631	0.0049	0.3949	0.0285	0.0455	0.0010	0.2987	722	169	338	21	287	6	83%
PSG3-44	14.4	69.4	99.3	0.70	0.0568	0.0053	0.3570	0.0348	0.0458	0.0012	0.2782	483	209	310	26	289	8	92%
PSG3-45	60.0	300	381	0.79	0.0538	0.0025	0.3455	0.0163	0.0462	0.0007	0.3171	365	112	301	12	291	4	96%
PSG3-46	11.1	50.0	84.0	0.60	0.0591	0.0048	0.3700	0.0299	0.0461	0.0011	0.3075	572	178	320	22	290	7	90%
PSG3-47	60.4	45.4	33.3	1.36	0.1050	0.0045	4.8545	0.2011	0.3347	0.0055	0.3984	1714	78	1794	35	1861	27	96%
PSG3-48	23.1	108	157	0.69	0.0514	0.0042	0.3426	0.0272	0.0486	0.0010	0.2521	261	185	299	21	306	6	97%
PSG3-49	18.5	91.0	116	0.79	0.0541	0.0049	0.3450	0.0290	0.0476	0.0010	0.2604	376	201	301	22	299	6	99%
PSG3-50	15.0	72.6	85.7	0.85	0.0686	0.0051	0.4166	0.0274	0.0458	0.0011	0.3583	887	154	354	20	289	7	79%
PSG3-51	25.9	132	116	1.15	0.0548	0.0045	0.3363	0.0279	0.0456	0.0010	0.2691	406	190	294	21	287	6	97%
PSG3-52	14.5	63.5	85.3	0.74	0.0576	0.0053	0.4062	0.0367	0.0514	0.0012	0.2646	522	203	346	26	323	8	93%
PSG3-53	43.5	228	221	1.03	0.0553	0.0038	0.3586	0.0248	0.0474	0.0010	0.2958	433	156	311	19	299	6	95%
PSG3-54	13.2	62.3	87.9	0.71	0.0564	0.0049	0.3554	0.0311	0.0460	0.0010	0.2516	478	193	309	23	290	6	93%
PSG3-55	124	659	404	1.63	0.0507	0.0025	0.3256	0.0157	0.0470	0.0008	0.3516	233	118	286	12	296	5	96%
PSG3-56	5.70	28.6	42.5	0.67	0.0769	0.0083	0.4345	0.0458	0.0460	0.0016	0.3291	1120	217	366	32	290	10	76%
PSG3-57	22.8	107	135	0.79	0.0549	0.0043	0.3381	0.0265	0.0454	0.0010	0.2706	409	169	296	20	286	6	96%
PSG3-58	16.1	74.8	106	0.70	0.0535	0.0050	0.3261	0.0280	0.0458	0.0011	0.2683	350	209	287	21	289	7	99%
PSG3-59	17.6	79.3	118	0.67	0.0574	0.0044	0.3652	0.0254	0.0477	0.0009	0.2776	509	201	316	19	300	6	94%
PSG3-60	21.8	92.1	128	0.72	0.0557	0.0044	0.3517	0.0257	0.0475	0.0012	0.3385	443	178	306	19	299	7	97%



**Table DR2.** XRD mineralogical composition of the Lower Permian samples from southeastern North China

Samples	Depth (m)	Quartz	Feldspar	Calcite	Siderite	Clay minerals	Clay mineral assemblage		
							Chlorite	Illite	Kaolinite
ps5	1460	34	0	0	2	64	35	25	40
ps7	1465	27	0	0	46	27	5	20	75
ps8	1470.5	33	0	0	6	61	15	35	50
ps9	1471.1	38	0	0	2	60	15	25	60
ps10	1473.9	38	2	0	3	57	20	20	60
ps11	1476.3	32	0	0	2	66	15	15	70
ps12	1477.2	30	2	0	2	66	15	20	65
ps13	1479.4	40	6	2	2	50	20	25	55
ps14	1480.5	33	3	0	3	61	25	25	50
ps15	1482.2	33	3	0	3	61	25	25	50
ps16	1482.4	34	3	0	2	61	20	20	60
ps17	1483.1	32	2	0	2	64	15	15	70
ps19	1484.7	34	0	0	0	66	15	15	70
ps20	1488.5	29	0	0	16	55	10	10	80
ps21	1490	32	2	0	4	62	20	20	60
ps26	1505	10	0	2	0	88	10	10	80
ps27	1506	14	0	0	0	86	15	10	75
ps28	1514.7	38	0	0	2	60	15	10	75
ps29	1518.6	32	2	0	0	66	15	5	80
ps30	1522.8	32	0	0	2	66	15	10	75
ps31	1524.5	4	0	0	0	96	10	10	80
ps33	1527	2	0	0	32	66	30	0	70
ps34	1529.5	46	0	0	5	49	20	5	75
ps35	1529.6	4	0	0	0	96	35	10	55
ps36	1531.5	24	0	0	0	76	65	20	15
ps37	1532	29	0	0	2	69	55	15	30
ps38	1535.6	29	2	0	0	69	25	25	50
ps42	1545	39	3	0	2	56	25	25	50
ps52	1564.8	34	2	0	0	64	25	25	50
ps53	1585	35	0	0	0	65	20	25	55
ps54	1587.7	40	2	0	2	56	15	25	60
ps55	1587.8	43	2	0	2	53	15	30	55
ps58	1590	35	2	0	2	61	10	20	70

**Table DR3.** Whole-rock major element (%) and trace element (ppm) geochemistry of the Lower Permian samples from southeastern North China

Sample	Depth (m)	Lithology	SiO <sub>2</sub>	Al <sub>2</sub> O <sub>3</sub>	Fe <sub>2</sub> O <sub>3</sub>	CaO	MgO	Na <sub>2</sub> O	K <sub>2</sub> O	TiO <sub>2</sub>	MnO	P <sub>2</sub> O <sub>5</sub>	LOI	Total	Rb	Sr	Ba	Zr
ps5	1460	mudstone	57.02	24.15	5.1	0.16	0.67	0.45	1.61	0.91	0.01	0.04	9.77	99.94	91.8	122.5	464	196
ps7	1465	siltstone	28.97	8.13	37.47	1.04	1.21	0.29	0.63	0.38	0.43	0.171	21.3	100.05	36.8	66.2	216	163
ps8	1470.5	mudstone	54.39	20.58	8.68	0.22	0.76	0.53	2.39	0.83	0.3	0.062	10.6	99.42	150.5	119.5	630	185
ps9	1471.1	mudstone	61.38	21.06	4.71	0.14	0.76	0.55	2.32	0.97	0.13	0.041	7.89	100	139	109.5	581	216
ps10	1473.9	mudstone	59.23	21.15	5.63	0.28	0.85	0.53	2.01	0.98	0.07	0.139	8.92	99.85	119.5	121	500	246
ps11	1476.3	mudstone	55.47	26.15	3.36	0.14	0.56	0.49	1.65	0.85	0.01	0.063	10.75	99.56	91.8	149	512	169
ps12	1477.2	mudstone	54.45	27.14	3.16	0.15	0.52	0.52	1.46	0.79	0.01	0.054	11.65	99.95	82.9	138	503	165
ps13	1479.4	siltstone	63.8	20.58	2.77	0.35	0.73	1.07	1.77	0.94	0.01	0.074	7.37	99.53	91.7	145	471	367
ps14	1480.5	siltstone	58.79	21.45	5.02	0.35	1.06	0.84	2.23	0.88	0.09	0.083	9.07	99.95	113.5	149.5	566	196
ps15	1482.2	mudstone	59	19.83	6.07	0.57	1.06	0.89	2	0.84	0.11	0.099	9.13	99.66	99.6	138.5	489	215
ps16	1482.4	mudstone	58.3	22.2	4.03	0.31	0.93	0.8	2.23	0.91	0.05	0.083	9.23	99.14	115	157.5	573	216
ps17	1483.1	mudstone	60.29	23.96	2.32	0.17	0.61	0.58	2.16	0.99	0.01	0.043	8.76	99.95	94.2	147	510	225
ps19	1484.7	mudstone	56.19	27	2	0.14	0.4	0.51	1.22	0.79	0.01	0.028	11.35	99.69	50.4	149.5	419	184
ps20	1488.5	mudstone	46.74	18.9	14.79	0.38	0.86	0.57	1.49	0.82	0.19	0.139	14.55	99.49	68.6	169.5	421	293
ps21	1490	mudstone	58.46	20.56	5.71	0.28	0.85	0.68	1.84	0.87	0.08	0.122	10.4	99.91	84.8	169.5	457	243
ps26	1505	mudstone	38.09	26.81	2.48	0.2	0.43	0.41	0.54	0.53	0.01	0.029	29.6	99.17	23.1	140.5	327	231
ps27	1506	mudstone	41.13	28.87	2.05	0.15	0.42	0.46	0.63	0.58	0.01	0.027	24.6	98.97	26.4	156.5	373	253
ps28	1514.7	mudstone	62.11	22.58	3.29	0.1	0.45	0.45	1.12	1.05	0.01	0.053	8.57	99.84	58.6	130.5	375	374
ps29	1518.6	mudstone	53.75	30.38	1.65	0.12	0.22	0.38	0.42	0.99	0.01	0.032	12.1	100.1	19.3	140	263	313
ps30	1522.8	mudstone	58.21	25.44	3	0.08	0.37	0.3	1.17	1.03	0.03	0.054	9.8	99.56	63.6	162	319	277
ps31	1524.5	mudstone	44.5	37.33	1.33	0.08	0.24	0.31	0.95	0.99	0.01	0.061	13.85	99.69	40.6	186	385	335
ps33	1527	mudstone	32.22	27.56	19.32	0.13	0.34	0.16	0.18	1.01	0.16	0.033	18.25	99.39	8.2	78.4	103	411
ps34	1529.5	mudstone	67.09	18.4	4.48	0.03	0.19	0.13	0.27	0.65	0.02	0.033	7.88	99.18	11.5	74	103.5	310
ps35	1529.6	mudstone	42.34	35.51	5.65	0.26	0.22	0.22	0.33	1.35	0.01	0.243	13.5	99.67	15.2	205	273	583
ps36	1531.5	mudstone	48.17	23.79	16.36	0.18	0.81	0.33	1.15	0.86	0.01	0.196	7.72	99.65	53.6	351	374	231
ps37	1532	mudstone	51.02	23.73	12.35	0.14	0.68	0.25	1.11	0.84	0.02	0.12	9.09	99.41	53.1	230	312	252
ps38	1535.6	mudstone	56.98	25.51	3.04	0.19	0.63	0.76	1.52	0.98	0.01	0.081	9.71	99.49	60	253	713	412
ps41	1538	fine-grained	63.02	20.29	3.25	0.91	0.7	1.8	1.96	0.75	0.01	0.132	6.96	99.89	65.9	265	704	207
ps42	1545	mudstone	60.76	23.51	1.98	0.08	0.49	0.75	1.8	0.9	0.01	0.048	8.98	99.39	83.9	171.5	551	296
ps52	1564.8	mudstone	53.63	26.74	1.48	0.07	0.49	0.69	1.94	0.74	0.01	0.056	13.85	99.74	89.5	130.5	431	210
ps53	1585	mudstone	46.65	23.11	1.32	0.07	0.39	0.43	1.37	0.72	0.01	0.071	25.5	99.68	65.9	142.5	285	224
ps54	1587.7	mudstone	62.46	23.16	1.17	0.1	0.36	0.44	2.06	0.91	0.01	0.027	8.96	99.71	79.3	121	526	482
ps55	1587.8	mudstone	62.32	22.4	1.29	0.12	0.37	0.4	2.14	1.02	0.01	0.031	9.13	99.29	83.3	119.5	520	579
ps58	1590	mudstone	60.55	22.12	1.31	0.05	0.4	0.4	1.88	0.69	0.01	0.038	12.35	99.85	68.5	94.9	432	279
ps60	1594.5	fine-grained	50.49	15.18	12.91	1.09	1.79	0.84	2.09	0.65	0.29	0.132	13.8	99.35	81.8	199	492	274

Figure DR1

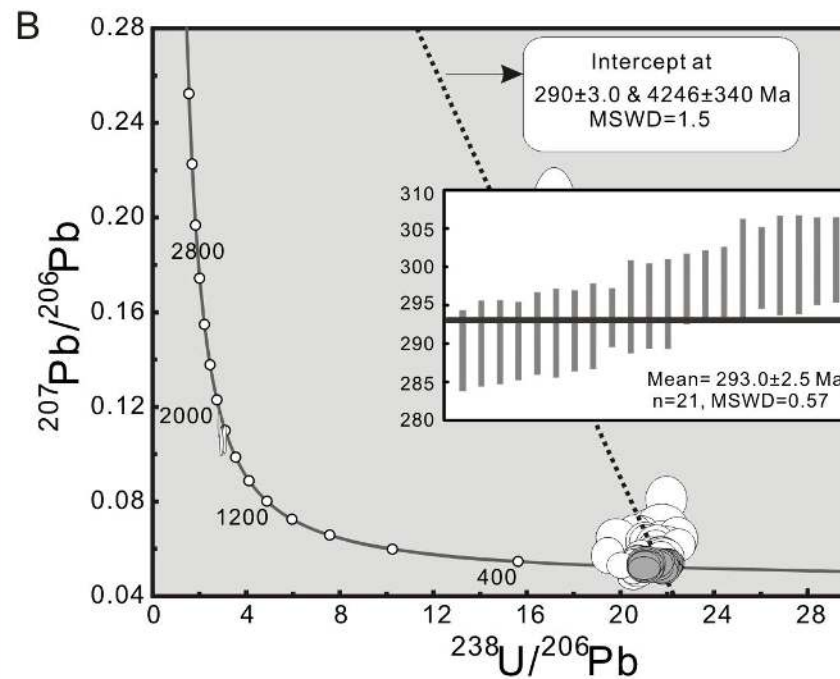
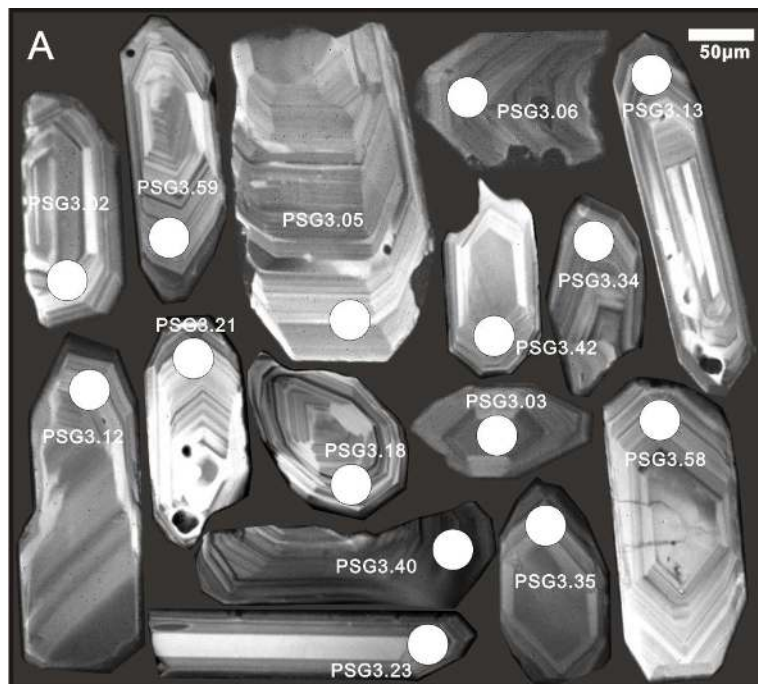


Figure DR2

